OpenFOAM® Journal

Volume 3 [Full papers], Pages 49–65
ISSN: 2753-8168

Hybrid LES/RANS Simulations of a 90° Pipe Bend Using Different CFD Solvers

A. Ekat[1,*], A. Weissenbrunner[1], M. Straka[1], T. Eichler[1], and K. Oberleithner[2]
Email address: ann-kathrin.ekat@ptb.de

[1]Physikalisch-Technische Bundesanstalt, Abbestr. 2-12, 10587 Berlin, Germany

[2] Institute of Fluid Dynamics and Technical Acoustics, Technische Universität Berlin, Müller-Breslau-Straße 8, 10623 Berlin, Germany

DOI: 10.51560/ofj.v3.36
Results with version(s): OpenFOAM® v1812
Repository:

Abstract. In this study we investigate the performance of several RANS and hybrid LES/RANS turbulence models using different CFD solvers (ANSYS Fluent, OpenFOAM and RapidCFD).The comparison is realised on the basis of predicting the flow development downstream of a 90° bend, with a focus on time-averaged velocity profiles up to approximately 31 times the pipe diameter D. The turbulence models accuracy is evaluated by means of performance indicators and velocity profiles in comparison to LDA measurements. It is demonstrated that all solvers produce the same results when the equal RANS model and numerical schemes are used. Additionally the results demonstrate that the use of RANS models is suitable as long as the location of interest is in the vicinity of the bend up to approximately 10 D downstream of the bend. With increasing distance, the accuracy of the RANS models decreases, and the use of hybrid LES/RANS models is recommended.
Additionally the performance of three hybrid LES/RANS models is investigated: the stress-blended eddy simulation (SBES) model as well as the Spalart-Allmaras-based and the k-ω SST-based improved delayed detached eddy simulation (IDDES) models. All three models show enhanced results for a distance to the bend greater than 10 D. Additionally, it is found that in this geometry configuration, the IDDES models require a transient inlet in OpenFOAM and RapidCFD. The flow separation due to the redirection inside the bend is too weak to generate turbulent fluctuations and a fast transition to full LES mode in the separation region. Due to the turbulent excitation at the inlet, the RANS region downstream of the bend is distinctly reduced, resulting in an enhanced performance of the hybrid IDDES models.

1. Introduction

Among the most popular solvers for computational fluid dynamics (CFD) in engineering are ANSYS Fluent (Fluent), a commercial and user-friendly software package, and OpenFOAM (OF), an open source code. Fluent offers customer software support and a detailed user's guide, but comes at high licence costs. In contrast, OF is free of charge and offers full access to the source code. It can be modified and expanded for personal needs.
Although both solvers are based on the finite volume method, they differ in details of the numerics. Fluent and OF feature most state-of-the-art turbulence models, including several Reynolds-averaged Navier Stokes (RANS), large eddy simulation (LES) as well as hybrid LES/RANS models, but again differ in details of the physical modelling.
A comparison of the Fluent and OF solvers was performed by Welahettige and Vaagsaether [1]. Employing RANS simulations, they investigated a gas-gas mixing process and found a higher mixing level for OF due to higher predicted turbulence kinetic energy and diffusive properties. Also Balogh et al. [2] compared the performance of Fluent and OF by RANS simulations of an atmospheric boundary layer over complex terrains and found that OF showed better results, with the constraint that the authors could not ensure the perfect consistency of the turbulence models. Moreover, Lysenko et al. [3] analysed

* Corresponding author

Received: 8 February 2021, Accepted: 12 September 2022, Published: 16 May 2023

several turbulent separated bluff-body problems with Fluent and OF using an unsteady RANS approach. They found a good agreement between the results of the different solvers. Although different authors compared the performance of the solvers OF and Fluent, no conclusive statement can be drawn, since they yield different results. The main reason for the different results of OF and Fluent in the first two mentioned references is probably due to different solver settings. In the present study the solver settings are defined in an equal manner and the comparison is extended by the solver RapidCFD [4, 5] (RCFD) that is shortly introduced in the next paragraph.

RCFD is a modified version of OpenFOAM 2.3.1 [6] from 2014 which works fully on graphical processor units (GPUs). Due to the porting process, it features fewer linear solvers, turbulence models as well as boundary conditions than more recent versions of OF. Reasonable results with RANS models are shown by Nocente et al. [7] and Molinero et al. [8] for simulations of turbo-machinery and for a high speed flow by Kurashov [9]. These studies showed a remarkable increase in speed of up to nine times compared to CPU-based solvers, which makes GPU-ported solvers an attractive tool for solving computationally expensive CFD problems.

Part of the present study is a comparison of the three above-mentioned CFD solvers by means of RANS simulations. The test case used is the flow inside and downstream of a 90° pipe bend. The flow inside the bend is redirected, yielding centrifugal forces that cause a shift of the core flow to the outer part of the bend. This leads to a deflection of the outer fluid particles along the pipe wall towards the inner part of the bend, resulting in two counterrotating secondary swirls being superimposed on the streamwise axial flow. These structures are called Dean vortices [10] and remain downstream of the bend.

The flow characteristics downstream of a 90° bend are important, as this structural element is commonly used in piping systems. The previously described flow conditions impose demands on flow meters installed downstream of non-straight pipe installations, as they are generally calibrated for fully developed turbulent flows [11–16]. Based on the knowledge of the disturbed velocity profile gained from CFD simulations, correction algorithms for measurement devices can be developed. To enhance the acceptance of such simulation-based algorithms, the accuracy and reliability of CFD simulations is of great importance. It is well known that RANS models are less accurate than LES models in the prediction of secondary flow. Although pure LES is feasible for large computational domains and high Reynolds numbers, it demands high computational costs regarding hardware and time. To optimise the computational cost and the accuracy, hybrid LES/RANS models can be used. They combine RANS in the wall region and LES in the core flow. Various hybrid LES/RANS models can be developed by changing the underlying turbulence models, as well as the size and location of the RANS regions and the transition from RANS to LES. An overview of different hybrid approaches is given, for example, in Fröhlich and Terzi [17]. However, it is still not clear which combination of CFD solver and turbulence model is appropriate for a specific application. In the present work, 90° pipe bend flow simulations are performed with combinations of solvers and turbulence models to assess their accuracy. An overview of the conducted simulations is given in Tab. 1.

There have been several investigations on the flow inside and downstream of a 90° bend, ranging from CFD [18–25] to experimental studies [26–30]. Most of the investigations mainly focus on the flow inside or in the vicinity of the bend. From the experimental studies it is known that the induced disturbances are maintained downstream for a distance greater than 31 times the pipe's diameter D [30]. Therefore, in this paper, simulations of a 90° bend with a downstream pipe with a length of 42 times the pipe's diameter D are conducted as $31\,D$ corresponds to the last recorded plane in the experiment. Results of simulations with the Fluent, OF and RCFD solvers using five different RANS and three hybrid LES/RANS models are compared to laser Doppler anemometry (LDA) measurements by Straka et al. [30] at six cross-sectional planes. To quantify the accuracy of the simulations, the L^2_{error} of the difference of the mean axial velocity profiles between the measurement and simulation data is calculated. Furthermore, the rotation strength of the Dean vortices and the decay of this secondary motion with increasing distance to the 90° bend are studied.

The paper is structured as follows: Firstly the simulation setup is described. It includes turbulence modelling and the geometrical and numerical setup. Afterwards the performance indicators used to assess the accuracy of the turbulence models are described. This is followed by the results and discussion of the simulation outcome, which is divided into two focus areas. At first it is shown that the three tested CFD solvers, Fluent, OF and RCFD, yield similar results on the basis of RANS simulations. Later, the performance of the turbulence models (RANS and hybrid LES/RANS) is evaluated.

2. Simulation setup

2.1. **Turbulence modelling.** Incompressible and isothermal flow motion can be described by the equations for the conservation of mass and momentum. The spatial and temporal resolution must be the size of the smallest turbulent fluid structures in the flow to perform direct numerical simulations (DNS). As DNS is not feasible for complex industrial applications, turbulence models are used to model the influence of these turbulent structures on the mean/filtered flow field by adding a turbulent viscosity ν_t (Boussinesq hypothesis). While RANS turbulence models resolve the mean flow characteristics only, LES turbulence models resolve large flow structures. For both, the structure of the incompressible averaged/filtered conservation equations is equal and reads in Einstein notation

$$\frac{\partial \bar{u}_i}{\partial x_i} = 0 \tag{1}$$

and

$$\frac{\partial \bar{u}_i}{\partial t} + \bar{u}_j \frac{\partial \bar{u}_i}{\partial x_j} = -\frac{1}{\rho}\frac{\partial \bar{p}}{\partial x_i} + \frac{\partial}{\partial x_j}\left[(\nu + \nu_t)\frac{\partial \bar{u}_i}{\partial x_j}\right], \tag{2}$$

with $u_i = (u, v, w)$ being the velocity vector, $x_i = (x, y, z)$ being the Cartesian coordinate vector and p the pressure; ρ and ν are the fluid's density and kinematic viscosity, respectively. An overbar denotes a Reynolds-averaged (RANS) or spatial filtered (LES) quantity. Gravity is not considered in this study. For further details on general CFD terminology and turbulence modelling, the reader is referred to, for example, Wilcox [31].

For a comparison of the solvers' performance, the k-ω shear stress transport (SST) [32] and the Spalart-Allmaras (SA) [33] RANS turbulence models are used. They are compared as the tested hybrid models are based on them. Additionally, different variants of the k-ε model are tested in OF (standard, realizable and Re-Normalisation Group (RNG)). The standard k-ε model is tested in high and low Reynolds wall treatment. Furthermore, the k-ω model is used. The purpose of testing different RANS models in OF is to show the performance of different RANS models. As the equal performance of the three solvers is already shown by means of the SA and SST model, a realisation on all solvers is redundant. An overview of the realised combinations of turbulence models and solvers is given in Tab. 1.

Table 1. Performed simulations.

Turbulence Model	OpenFOAM	ANSYS Fluent	RapidCFD
Spalart-Allmaras	✓	✓	✓
k-ω SST	✓	✓	-
k-ω	✓	-	-
standard k-ε	✓	-	-
realizable k-ε	✓	-	-
RNG k-ε	✓	-	-
SBES	-	✓	-
SST-IDDES	✓	-	-
SA-IDDES	-	-	✓

2.1.1. *Stress-blended eddy simulation turbulence model.* The stress-blended eddy simulation turbulence (SBES) model is a hybrid LES/RANS method implemented in Fluent. It was set up using the SST RANS model with standard coefficients, the Smagorinsky-Lilly LES sub-grid model [34] with a Smagorinsky constant of $C_S = 0.1$ and solver settings in accordance with Menter's recommendations for wall-modelled LES [35]. In its incompressible form, the turbulent viscosity ν_t for the SBES model is calculated by

$$\nu_t^{\mathrm{SBES}} = f\,\nu_t^{\mathrm{RANS}} + (1-f)\,\nu_t^{\mathrm{LES}}, \quad 0 \le f \le 1 \quad , \tag{3}$$

with ν_t^{RANS} and ν_t^{LES} being the turbulent viscosity based on the underlying RANS and LES model, respectively. In a transient run, both ν_t^{RANS} and ν_t^{LES} are calculated on the entire domain. A blending function f is required to specify in which parts they are applied. Here, we used a location-dependent blending function which is implemented with user defined function (UDF) in Fluent. This function was defined and empirically verified for a segmental orifice plate (disturbance generator for the emulation of a 90° bend) in Straka et al. [36]. It tends towards zero with an increasing distance from the wall, resulting in $\nu_t^{\mathrm{SBES}} \sim \nu_t^{\mathrm{LES}}$ in the core flow.

Although two additional equations need to be calculated on the entire mesh beyond the equation of the LES model, the main benefit by means of computational cost is in the reduced grid size due to a coarser scaling in the near wall region, as this part is covered by the RANS approach.

2.1.2. *Improved delayed detached eddy simulation model.* While the SBES model blends ν_t^{RANS} and ν_t^{LES} based on the distance from the wall, for the improved delayed detached eddy simulation (IDDES) models, the transport equations of the turbulence quantities of the RANS models are modified themselves. For the SA-based IDDES model, the original length scale in the destruction term is modified, yielding a decreased turbulent viscosity ν_t as the length scale decreases [37]. For the SST version of the IDDES model, the length scale in the dissipation term of the transport equation for the turbulence kinetic energy k is modified, also leading to a reduced turbulent viscosity ν_t as the turbulent length scale is decreased [38]. For both model variants, the turbulent length scale is calculated based on

$$l_{\mathrm{IDDES}} = \tilde{f}_d \, (1 + f_e) \, l_{\mathrm{RANS}} + \left(1 - \tilde{f}_d\right) \, l_{\mathrm{LES}}. \tag{4}$$

The empirical blending function $\tilde{f}_d$ is dependent on the normal distance to the closest wall d_w and the maximum local grid spacing $h_{\max}$, ensuring RANS mode in the vicinity of the wall. The other empirical blending function f_e prevents a log-layer mismatch at the RANS and LES interface. According to Gritskevich et al. [38], it can be set to zero for the SST variant of the model. For further details on these two models, the reader is referred to Shur et al. [37] for the SA-based version and Gritskevich et al. [38] for the SST-based IDDES model version.

2.2. **Geometrical domain and mesh generation.** The geometry and fluid properties are chosen according to the experimental setup of the LDA measurements conducted in Straka et al. [30]. In the experiment, the streamwise axial velocity component w (z-direction in Cartesian coordinates) and the non-axial velocity component u (x-direction in Cartesian coordinates) are recorded at 303 measurement points per plane with an expanded uncertainty of 0.5 % (k = 2) [39]. In total the velocity profiles at six planes with increasing distance to the outlet of the bend are acquired. They are labelled as a multiple of the pipe's diameter D, namely $2.43\,D$, $5.56\,D$, $10.7\,D$, $15.69\,D$, $20.82\,D$ and $30.82\,D$. A fully developed turbulent flow upstream of the bend is ensured in the experiment by a $\sim 95\,D$ long straight smooth pipeline.

The fluid under study is water at 30 °C. The Reynolds number is $Re = 50\,000$, based on the pipe's diameter $D = 0.1\,\mathrm{m}$, and the mean averaged velocity $w_{\mathrm{vol}} = 0.40035\,\mathrm{m/s}$.

The bend has a curvature radius of $r_k = 1.425\,D$. In the geometrical domain of the simulation, the bend is connected to straight pipes with a length of 7 times the pipe's diameter D upstream and $42\,D$ downstream, respectively (see Fig. 1). Downstream of the bend, the wall facing the positive x-direction is referred as the inner wall, and the one facing the negative x-direction as the outer wall. The additional domain length was chosen to ensure that the results are not influenced by the inlet and outlet boundary conditions.

For the mesh generation, the commercial ANSYS ICEM CFD 19.3 [40] software is used. All the meshes

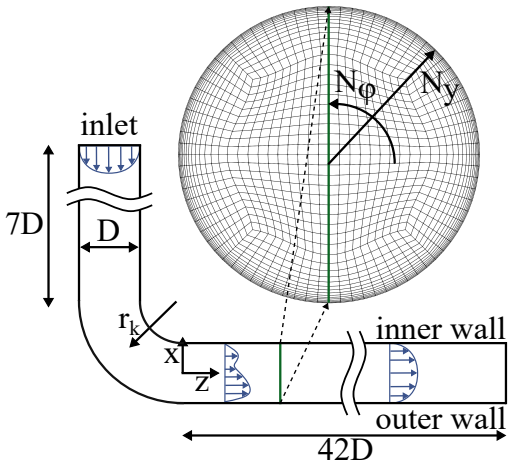

Figure 1. Cross-sectional grid structure. Counting direction of mesh elements in the radial direction N_y and the circumferential direction N_ϕ indicated by arrows. The green line corresponds to the path where the maximum horizontal velocity, as well as the investigated velocity profiles are detected. 'Horizontal' is in accordance with the orientation in the LDA measurements [30], where the marked xz-plane is parallel to the ground.

are structured hexahedral O-grids, as illustrated in Fig. 1. Mesh independence is studied by changing the grid resolution in three steps by increasing the number of cells in the circumferential direction N_ϕ, the radial direction N_y and the axial direction N_z. The medium resolution mesh is based on general guidelines for mesh generation, the finer and coarser meshes were adjusted according to this resolution. The height of the first cell close to the wall is set to correspond to a dimensionless wall distance of $y^+ \sim 2.5$. Additionally, the medium resolution meshes are tested with a dimensionless wall distance of $y^+ \sim 0.25$. These y^+-values are calculated based on the assumption of a fully developed pipe flow. The results of the CFD simulations yield y^+ values of average 3 (max. 7) and 0.3 (max. 0.6), respectively, for the used grid resolutions. While the average is approximately constant for all turbulence models, the maximum value varies. The given value corresponds to the maximum value of all simulations. Still this one is in the valid range for the usage of continuous wall functions. The quality of the grids is evaluated based on ANSYS ICEM CFD's criteria *Quality* and *Aspect Ratio* [40]. The minimum quality of the poorest cell $Quality_{\min}$ and the maximal aspect ratio $AR_{\max}$ are included for each mesh in Tab. 2. Too save computational costs and also due to asymmetric profiles of RANS simulations with the SST model (see Section 4), for each resolution step, there is a RANS mesh covering the entire domain (mesh type b) and half of it applying a symmetry plane (mesh type c). This symmetry plane is in the xz-plane cutting the origin of the Cartesian coordinate system. Due to RCFD's inability to handle symmetric boundary conditions the RANS mesh covering the entire domain (mesh type b) is necessary. In each resolution step, the difference in the RANS (b and c) and hybrid (a) mesh is mainly in the resolution in the axial direction N_z. Additionally, there is a mesh to test the k-ε model with a wall function (mesh2d) and a mesh with an expanded upstream pipe of $50\,D$ to investigate the influence of transient turbulent fluctuations at the inlet on the IDDES models (mesh2e). All grids are summarised in Tab. 2.

Table 2. Grid parameters.

name	$N_{\text{hexa}}/10^6$	$Quality_{\min}$	$AR_{\max}$	N_ϕ	N_z/D	N_y	y^+	domain	description	Δt [s]
1a	1.97	0.732	19.2	80	25	30	2.5	full	coarse	0.0025
1b	1.15	0.725	47.7	80	10 - 25	23	2.5	full	coarse	-
1c	0.61	0.732	49.5	80	10 - 25	30	2.5	half	coarse	-
2a	5.75	0.798	14.1	120	35	35	2.5	full	medium	0.002
2b	2.94	0.799	48.4	120	10 - 35	35	2.5	full	medium	-
2c	1.48	0.798	49.7	120	10 - 35	35	2.5	half	medium	-
2d	1.61	0.796	6.45	120	10 - 35	22	30	full	medium	-
2e	10.63	0.796	14.6	120	35	35	2.5	full	medium	0.002
3a	8.79	0.798	141	120	35	49	0.25	full	medium	0.002
3b	4.49	0.799	484	120	10 - 35	49	0.25	full	medium	-
3c	2.26	0.798	479	120	10 - 35	49	0.25	half	medium	-
4a	19.92	0.794	9.8	200	50	42	2.5	full	fine	0.001
4b	8.31	0.794	48.9	200	10 - 50	51	2.5	full	fine	-
4c	4.20	0.799	49.8	200	10 - 50	42	2.5	half	fine	-

2.3. **Numerical setup.** To create comparable results, similar choices for the numerical setup were made. Despite having slightly different discretisation schemes for time and space that are available at the specific solvers, only the second-order accurate numerical schemes are chosen for the present simulations. For the momentum equation we used the linear scheme (central difference) for all solvers. For the turbulent quantities different high resolution divergence schemes were used for specific solvers, which is not critical for scale resolving simulations [35, 41]. The time step for the transient simulations was chosen to stick to a maximal Courant number of 1 ($CFL_{\max} < 1$) yielding the time steps listed in Tab. 2. The averaging process starts at 12 s so that the flow passes the whole domain once before the averaging starts. Due to the larger computational domain of mesh2e, the averaging process starts at 24 s for this mesh The averaging time for the transient simulations is 60 s. This averaging interval was set as the change in the results for longer averaging intervals is smalls. This was evaluated for the SA-IDDES turbulence model on mesh2a and mesh2e in RCFD. For both cases the simulations were performed for an averaging interval of 180 s. The change of the L^2_{error} over time can be found in Fig. 11.

The non-linear equation system is solved using the SIMPLE algorithm for the steady-state simulations and the PIMPLE algorithm (OF-algorithm based on SIMPLE and PISO algorithm; OF and RCFD) and the transient SIMPLE algorithm (Fluent) for the transient simulations.

The simulations with the SBES hybrid model are conducted with the ANSYS Fluent Release 19.3 software

[42]. The IDDES models are performed on OpenFOAM®v1812 [43] (SST-based) and RapidCFD [4] (SA-based), with default settings defined in the respective CFD solver.

2.4. **Boundary conditions.** For the RANS simulations, a mean fully developed turbulent flow profile is prescribed at the inlet. Velocity components and turbulence quantities are specified at the inlet taken from precursor simulations. This is done as a length of $7\,D$ wouldn't be enough to achieve a fully developed velocity profile from a mean flow rate. This approach is used for the IDDES models as well, as done by Shur et al. in [37] for the backward-facing step for the SA-IDDES hybrid model. The IDDES model should work in RANS mode in the attached boundary layer upstream of the bend and is supposed to switch to LES mode due to the separation downstream of the bend in the core flow.
Additionally, it was tested whether a turbulent transient inlet condition influences the results with the IDDES models. Initial investigations with OF's/RCFD's *turbulentInlet* with a *fluctuationScale* of (0.4 0.1 0.1) are presented. This boundary condition generates a random fluctuating inlet condition by adding a fluctuation to a mean field. As only random perturbation is prescribed, the pipe's length upstream of the bend was extended to a total length of $50\,D$. This ensures that the fluctuations develop towards a realistic fully turbulent profile entering the bend.
For the SBES model, a turbulent, unsteady fluctuating boundary condition is required to cause reasonable results. Fluent's vortex method based on [44] is used to generate a turbulent, unsteady inlet condition.
The domain walls are assumed to be hydraulically smooth, and for the velocity, a no-slip boundary condition is chosen. For the turbulence kinetic energy k, a value of zero is set at the wall. The specific dissipation rate ω is calculated based on the dimensionless distance to the wall y^+ using the continuous wall function based on [45]. A continuous wall function was chosen for the dissipation of turbulent kinetic energy ε for the ε-based models as well. The turbulent viscosity ν_t is calculated from the other turbulence quantities for the two-equation models, whereas Spalding's continuous wall function [46] is used for the one-equation SA model.

3. Performance indicators

For a comparison of the agreement of the velocity profiles in the axial direction z on a cross-sectional plane, the percentage normalised L^2_{error} of the difference between measurement and simulation results is calculated according to

$$L^2_{\text{error}} := \sqrt{\frac{1}{A}\int^{A} (w^{\text{LDA}} - w^{\text{CFD}})^2 \,\mathrm{d}A} \;\cdot\; 100 \;\; \%, \tag{5}$$

where w^{LDA} and w^{CFD} denote the normalised mean axial velocity component of the LDA measurements and CFD simulations, respectively; A is the cross-sectional area of each plane. All reported velocity components are normalised by the spatial mean volumetric axial velocity w_{vol} of the CFD simulations and LDA measurements, respectively, due to little variations in $w^{\text{LDA}}_{\text{vol}}$.
The second evaluated performance indicator is the maximum horizontal velocity $u_{\max}$ [30]. It is an approximation of the swirling velocity of the Dean vortices. It is defined as the ratio of the maximal magnitude of the velocity component u along the horizontal path at $y = 0$ (depicted in green in Fig. 1) to the volumetric velocity in the axial direction w_{vol}. The equation reads

$$u_{\max} := \frac{\max(|u_{y=0}|)}{w_{\text{vol}}} \,. \tag{6}$$

Other authors use the swirl intensity I_S based on [47] to evaluate the swirling intensity of the Dean vortices. A modified version taking only one secondary component into account was analysed as well. It shows similar results to $u_{\max}$ and confirms the validity of $u_{\max}$ as a measure of the swirling intensity of the Dean vortices.

The performance indicators are examined at six downstream planes, with increasing distance to the bend, that correspond to the ones from the LDA measurements.

4. Results and discussion

4.1. **RANS turbulence models.** For the RANS simulations, the SST model shows no considerable grid dependence on the tested meshes. This is true for all CFD solvers used. For the SA model, a minor level of dependence on the near-wall grid resolution has been found. There are minor variations in the performance indicators and the velocity profiles, but they are negligible compared to the variations between the turbulence models. The results are included in Fig. 12.

For meshes covering the entire domain (mesh type b), it has been found that SST RANS simulations lead to asymmetric results for meshes of medium and fine resolution, using second-order accuracy for the space discretisation. This holds for all tested solvers. However, the reason for the asymmetric profiles has not been completely clarified.
To overcome this, grids covering half of the domain (section facing the positive y-direction) were generated and tested (mesh type c). As they mirror the domain, the result is forced to be symmetric. This approach was used for the SST model for the Fluent and OF solvers. RCFD does not feature the symmetric boundary condition and is therefore excluded.

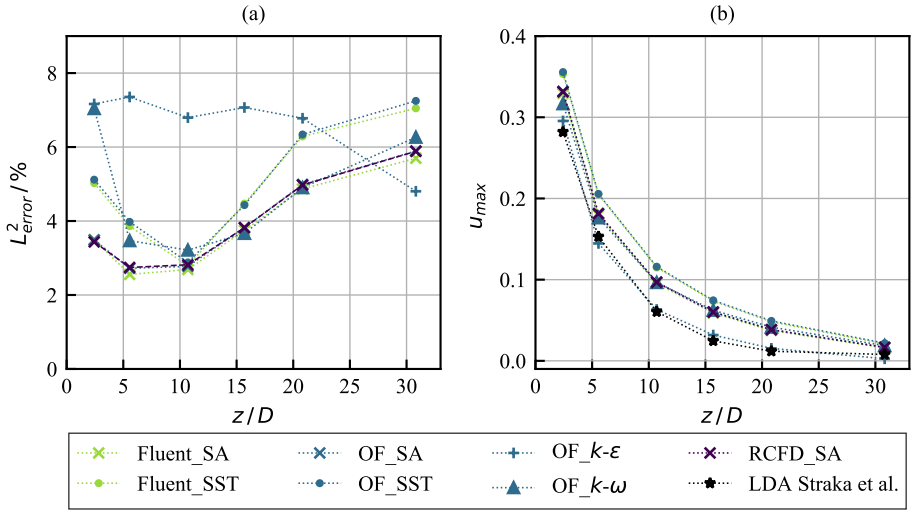

Figure 2. Comparison of CFD solvers and turbulence models. Mesh: 3b (SA, k-ε, k-ω) and 3c (SST). (a) L^2_{error} and (b) maximum horizontal velocity $u_{\max}$ over the normalised distance downstream of the bend z/D. For better visualisation, the values evaluated at the marked positions are connected by lines. LDA measurements by Straka et al. [30].

It is shown that the CFD solvers used (Fluent, OF and RCFD) generate comparable results. The performance indicators are illustrated for the SA and SST RANS turbulence models for the different solvers in Fig. 2. In (a), the percentage L^2_{error} is plotted over the normalised distance to the bend z/D, in (b), we see the maximum horizontal velocity $u_{\max}$. For both performance indicators, it is shown that there is a good agreement between the CFD solvers, and they produce similar results, using equal solver settings. The SA model shows the lowest values for the L^2_{error} with a value of about 3 % in the first three cross-sections in proximity to the bend (2.43 D to 10.7 D). From there on, the values increase proportionally to the distance to the bend up to 6 % at 30.81 D. The same course of the L^2_{error} is found for the SST and k-ω model. In the vicinity of the bend, the value decreases from 5 % and 7 %, respectively, to the lowest value of about 3 % at 10.7 D and increases with further distance to the bend. While the curve of the k-ω model overlaps with the one of the SA model, the values of the SST model are about 1 % higher.

The k-ε models differ the most from the other ones. This tendency has been found for all tested variants (standard version with high and low Re wall treatment, realizable, RNG). For reasons of clarity, only the results of the standard k-ε model (low Re wall treatment, mesh3b) are presented within the paper, as this model shows the best results by means of the performance indicator $u_{\max}$. The results of the other ε-based models are attached in Fig. 13. The L^2_{error} for the standard k-ε model is at a constant high level of about 7 % in a distance range from approximately 5 to 20 times the pipe's diameter D downstream of the bend. For the last evaluated plane, the value drops and shows the lowest value of about 4.5 %. The high values up to 20 D are mainly due to a steeper flow profile close to the wall and therefore a higher maximum velocity in the axial direction z, as can be seen in Fig. 3. In this figure, the profiles of the normalised axial velocity component w/w_{vol} at horizontal position $y = 0$ at six downstream positions (2.43 D ... 30.82 D) for the RANS turbulence models as well as the LDA measurement are plotted. It can be seen from this figure that the tested RANS models (except k-ε) show similar results for the flow profiles in the axial direction. All the models have in common that they underestimate the redirection of the axial flow profile towards a fully developed pipe profile compared to the LDA measurements. The focus of the core flow stays on the side of the outer wall (negative x-direction), leading to an increased

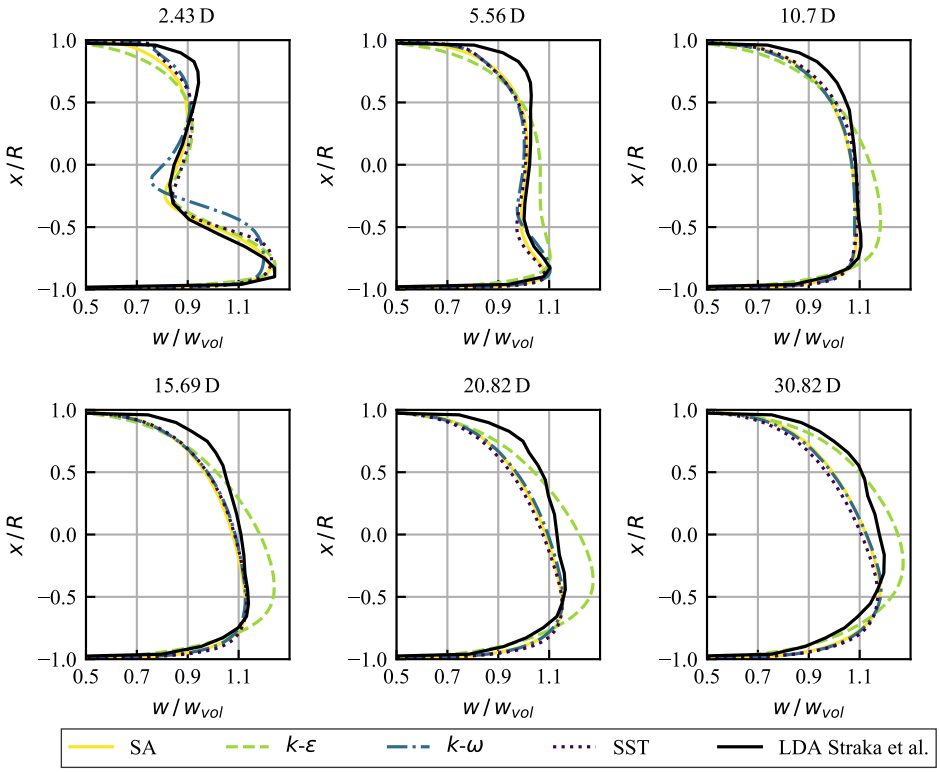

Figure 3. Comparison of RANS turbulence models. Flow profiles of the axial velocity component w normalised with the volumetric velocity w_{vol} at six axial positions downstream of the bend over the normalised radius x/R. Horizontal position $y = 0$. LDA measurements by Straka et al. [30].

L^2_{error} with a growing distance to the bend (see Fig. 2(a)).
The high L^2_{error} of the k-ω turbulence model in plane 2.43 D is mainly due to an underestimation of the displacement of the core flow towards the outer wall (negative x-direction) that is indicated in Fig. 3 (2.43 D).
With increasing distance to the bend, the swirling intensity of the Dean vortices decays. This is observable by the decreasing maximum horizontal velocity u_{max}, see Fig. 2(b). u_{max} is plotted over the normalised distance to the 90° pipe bend z/D for the four RANS turbulence models in comparison to the LDA measurements. While the k-ε model is in good agreement with the LDA measurement and follows its decay from 0.29 at position 2.43 D to 0.01 at position 30.81 D, the other models overpredict the maximum horizontal velocity u_{max} and therefore the swirling velocity of the Dean vortices.

4.2. **Hybrid LES/RANS models.** In the following, the results of the hybrid LES/RANS simulations are presented and discussed. The results of the hybrid models correspond to an averaging interval of 60 s, unless otherwise stated.

4.2.1. *Grid dependence.* In contrast to the RANS models, the hybrid models used do show grid dependence on the tested meshes. For the SBES model, it has been found that the near-wall resolution has an impact on the simulation results. For a smaller height of the first cell adjacent to the wall (mesh3a), the results are slightly improved, indicated by a decreased L^2_{error} by $\sim 0.5\,\%$ in each recorded plane, compared to a mesh with a coarser grid resolution in the vicinity of the wall (see Fig. 4 (a)). For all mesh resolutions, the L^2_{error} is the highest in the first two compared planes that are the closest to the bend. The value decreases till approximately 10 D downstream of the bend and stays nearly constant afterwards.
For the SST-IDDES model, no tendency has been found for the whole domain. While the mesh with a fine near-wall resolution gives better results for a distance to the bend smaller than 10 D regarding the L^2_{error}, the results are worse with a growing distance (Fig. 6 (a)), but the overall dependence is weak. For the SA-IDDES model, the grid dependence has been found for the last two recorded planes (Fig. 5 (a)).

In this region, the L^2_{error} of the results generated on the finest mesh (mesh4a) is higher than the ones of the other meshes. For the other recorded planes, the differences are less distinct. For the coarsest grid (mesh1a), the IDDES models, both the SA-based and SST-based, fail to give reasonable results. The errors are beyond 10 %. Therefore, the results are excluded from the figures.

The strength of the secondary Dean vortices is less influenced by the grid resolution. Considering

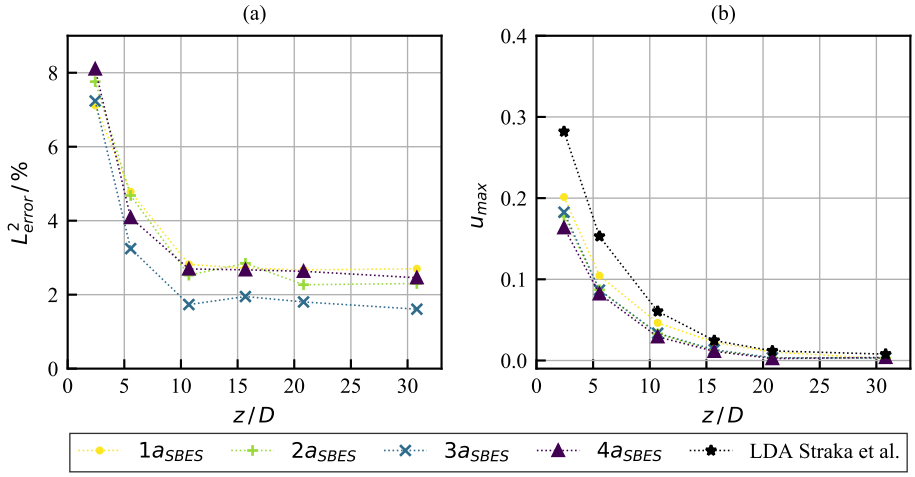

Figure 4. Comparison of different mesh resolutions according to Tab. 2. Turbulence model: SBES (a) L^2_{error} and (b) maximum horizontal velocity $u_{\max}$ over the normalised distance downstream of the bend z/D. For better visualisation, the values evaluated at the marked positions are connected by lines. LDA measurements by Straka et al. [30].

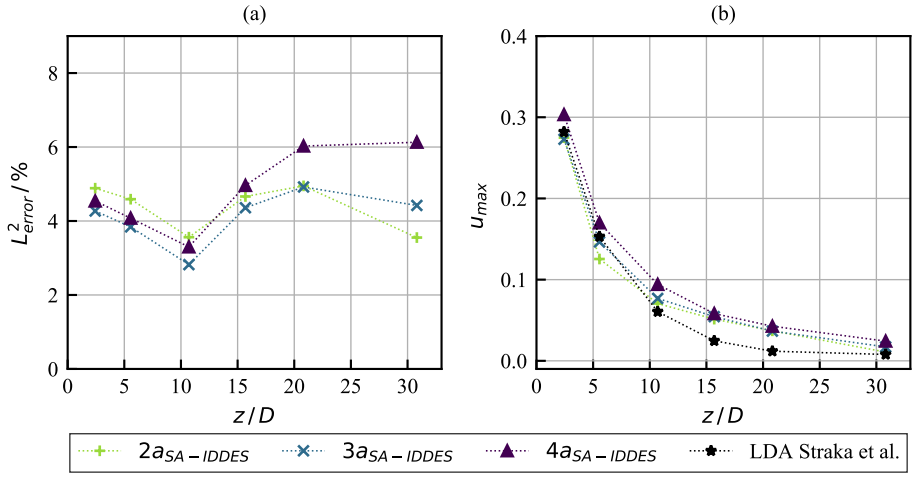

Figure 5. Comparison of different mesh resolutions according to Tab. 2. Turbulence model: SA-IDDES (a) L^2_{error} and (b) maximum horizontal velocity $u_{\max}$ over the normalised distance downstream of the bend z/D. For better visualisation, the values evaluated at the marked positions are connected by lines. LDA measurements by Straka et al. [30].

the maximum horizontal velocity $u_{\max}$ (Fig. 4 (b), Fig. 5 (b), Fig. 6 (b)), the grid dependence is less pronounced for all hybrid model variants.

4.2.2. *Comparison of turbulence models.* Despite these grid dependencies, distinct differences between the models have been found that surpass the influence of the grid. To better compare the models, the following reported results correspond to the medium resolution grid with a y^+-value of 2.5 (mesh2a). Comparing the contour plots of the normalised axial velocity w/w_{vol} for six downstream positions ($2.43\,D \ldots 30.82\,D$) of the tested hybrid LES/RANS models (Fig. 7), it can be seen that the SBES model

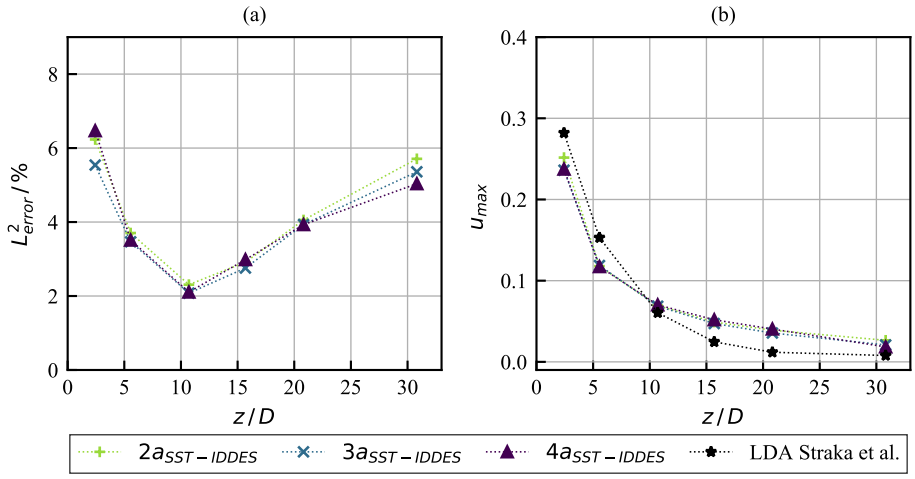

Figure 6. Comparison of different mesh resolutions according to Tab. 2. Turbulence model: SST-IDDES (a) L^2_{error} and (b) maximum horizontal velocity $u_{\max}$ over the normalised distance downstream of the bend z/D. For better visualisation, the values evaluated at the marked positions are connected by lines. LDA measurements by Straka et al. [30].

surpasses both IDDES model variants with a steady inlet conditions in a distance range from 10.7 D to 30.82 D. While the horseshoe shape, caused by the Dean vortices and the displacement of the core flow due to the centrifugal forces inside the bend, is still visible for the IDDES models with steady inlet up to a distance of 30.82 D, it is dissolved for the SBES model, and there is a good agreement between the simulation results and the LDA measurement.

Also in terms of the L^2_{error} (see Fig. 8 (a)), the good performance of the SBES model for a downstream distance to the bend greater than 10 D is observable. A L^2_{error} below 2 % denotes an accurate result, keeping in mind that L^2_{error} will not reach zero as there is still uncertainty in the measurements.

Regarding the L^2_{error}, the hybrid IDDES models with steady inlet conditions are less accurate with an increasing distance to the bend in the interval from approximately 10 to 31 D, especially in comparison to the SBES model. While all models show comparably good results at position 10.7 D, the results of the IDDES simulations and the LDA measurements deviate with a growing distance to the bend. This is caused by the inability of the IDDES models to re-form a fully developed flow profile and dissolve the secondary motion, illustrated in Fig. 9. For the IDDES models with a steady inlet condition, it is observed that the centroid of the velocity profile stays in the outer part of the pipe (negative x-direction), resulting in an increased L^2_{error}. There is nearly no difference to the results of the corresponding RANS models. For the SBES model, it has been found that with a growing distance from the bend ($z > 10\,D$), the w/w_{vol} flow profile converges towards the profile recorded in the LDA measurement and can hardly be distinguished from it. This differs close to the bend at the distance 2.43 D. At this downstream position, the SBES model shows the poorest results regarding the L^2_{error} of the tested hybrid LES/RANS models. This is mainly due to an underprediction of the displacement of the core flow towards the outer pipe wall (negative x-coordinates), as can be seen in Fig. 9 (2.43 D). In comparison, the flow profiles of the IDDES models in the first recorded plane (2.43 D) are similar in the magnitude and shape of the flow profile's maxima and similar to the LDA measurement.

While the tested RANS models tend to overpredict the maximum horizontal velocity $u_{\max}$, the hybrid LES/RANS models underpredict $u_{\max}$ in the distance range till approximately 10 D, see Fig. 8(b). In this area, the SA-IDDES model shows the best results. With a growing distance, the results of this model deviate from the LDA measurements. For $z/D > 10$, the maximum horizontal velocity $u_{\max}$ and therefore the rotation strength of the Dean vortices is higher for the SA-IDDES models than for the LDA measurement. The same tendency is found for the SST-IDDES hybrid model. As with the L^2_{error}, the SBES model shows inaccurate results regarding the maximum horizontal velocity $u_{\max}$ in the planes closest to the bend. The SBES model clearly underpredicts the rotation strength of the Dean vortices close to the bend. However, further downstream it approaches the value of the LDA measurements.

As a measure for the RANS and LES region, the value of the turbulent viscosity ν_t can be used. It is higher in the RANS region and tends towards zero at the wall. In Fig. 10, the turbulent viscosity

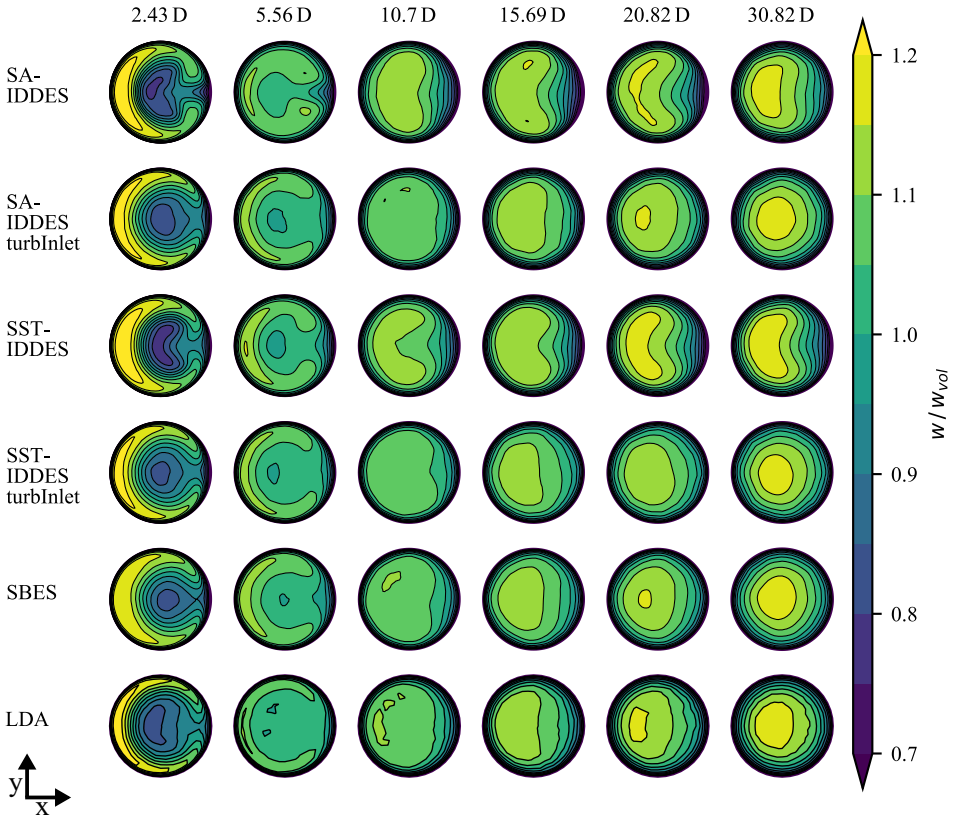

Figure 7. Contours of the axial velocity component w normalised with the volumetric velocity $w_{\text{vol}}^{\text{CFD}}$ and $w_{\text{vol}}^{\text{LDA}}$, respectively. Each column represents one downstream position with increasing distance to the bend as a multiple of the pipe's diameter D.

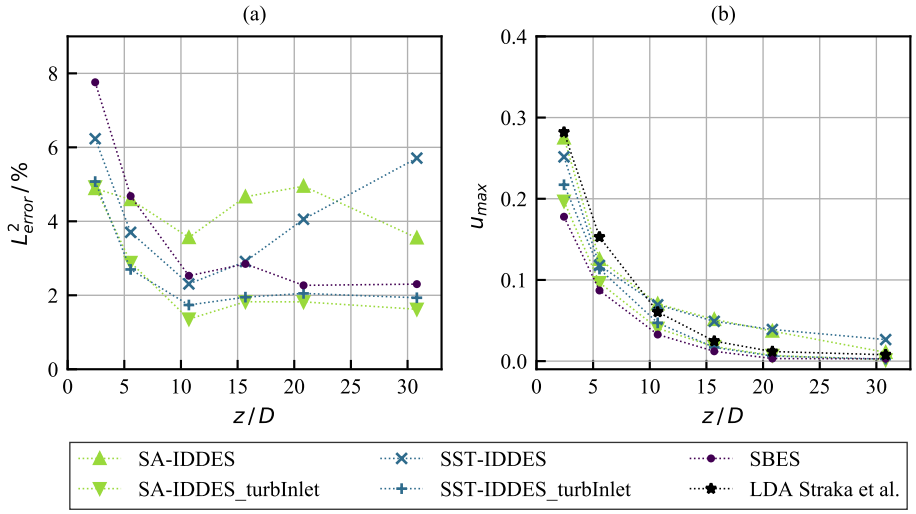

Figure 8. Comparison of hybrid LES/RANS turbulence models. Mesh: 2a. (a) L_{error}^2 and (b) maximum horizontal velocity u_{max} over the normalised distance downstream of the bend z/D. For better visualisation, the values evaluated at the marked positions are connected by lines. LDA measurements by Straka et al. [30].

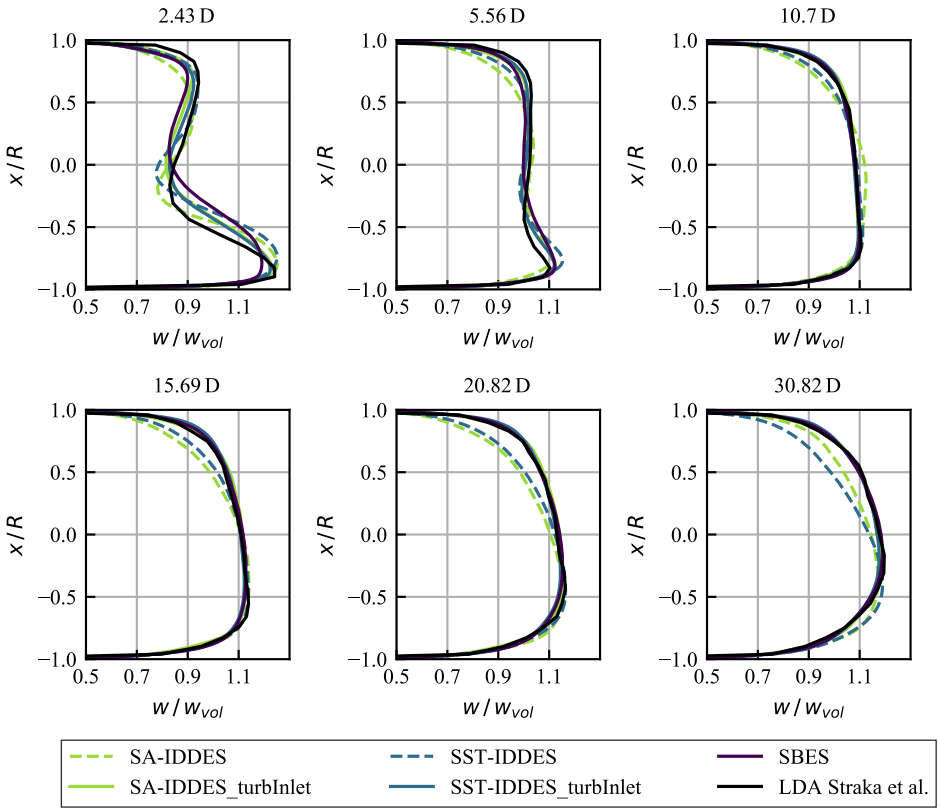

Figure 9. Comparison of different hybrid LES/RANS turbulence models. Flow profiles of the axial velocity component w normalised with the volumetric velocity w_{vol} at six axial positions downstream of the bend over the normalised radius x/R. Horizontal position $y = 0$. LDA measurements by Straka et al. [30].

ν_t over the normalised radius x/R at the horizontal position $y = 0$ for six downstream axial positions ($2.43\,D \ldots 30.81\,D$) is plotted. The values of the IDDES hybrid models correspond to the mean value, while the values of the SBES model correspond to the instantaneous values at a time step of 60 s. As this model has a fixed transition function from the RANS to the LES region, the lack of an averaged value is manageable, and the comparison is still meaningful.

In the vicinity of the 90° bend ($z = 2.43\,D$), both IDDES models with steady inlet conditions feature a large RANS region close to the wall. The RANS region covers approximately 2/3 of the cross-section area. Additionally, it can be observed that, for the same mesh resolution, the value of ν_t in full LES mode (core flow) has different values for the tested hybrid LES/RANS models. For the SBES model, the value is the lowest; for the SST-IDDES model, it is the highest (see Fig. 10). With an increasing distance to the bend, the value of ν_t of the SA-IDDES model in the LES region converges towards the one of the SBES model. Also, the size of the RANS region shrinks for this model with an increasing distance to the bend, and this model tends towards a wall-modelled LES. This results in a similar shape and height of the ν_t profiles over the normalised radius x/R at the distance $30.82\,D$ for the hybrid models SA-IDDES and SBES.

The RANS region of the SST-IDDES model does not shrink as fast as with the SA-IDDES model. Additionally, the value of ν_t in the LES region is at least four times higher than for the SBES model in all planes.

4.3. **Influence of inlet conditions on IDDES models.** All the previously presented results of the IDDES models correspond to a steady, fully developed inlet condition. In the following, the influence of an unsteady fluctuating inlet is discussed. To generate persistent fluctuating scales in OF and RCFD using the *turbulentInlet* boundary condition, high excitation at the inlet is required. Additionally, the turbulent viscosity ν_t for the SA-based model and the turbulence kinetic energy k for the SST-based model must be set to a low value at the inlet. Otherwise all prescribed fluctuations dissipate.

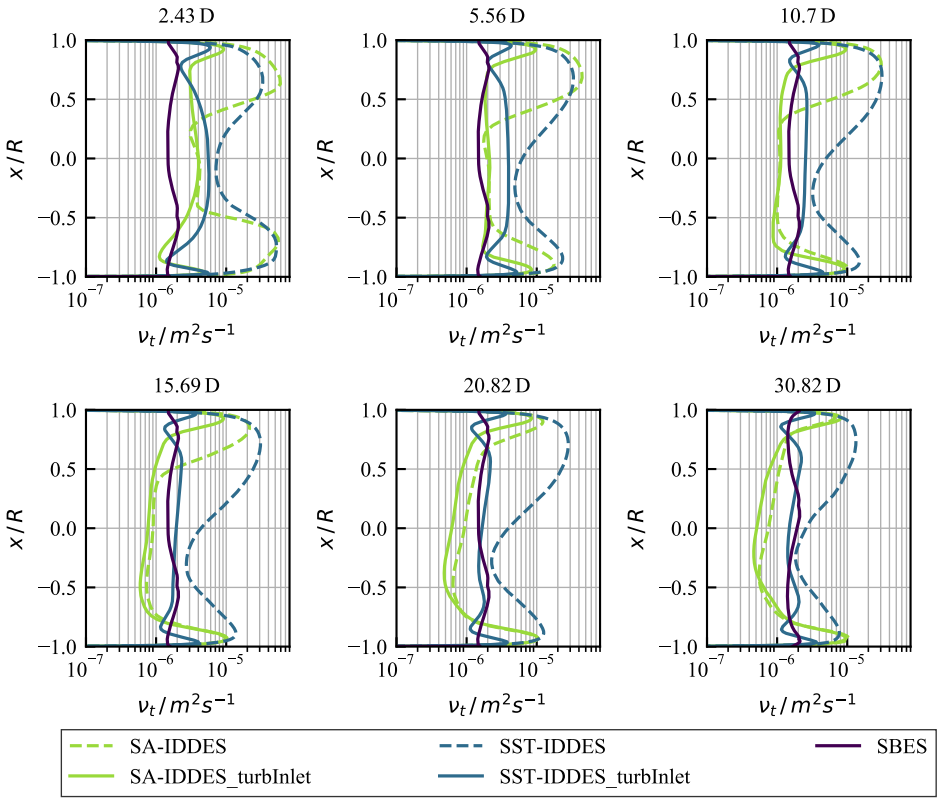

Figure 10. Turbulent viscosity ν_t over the normalised pipe radius x/R at horizontal position $y = 0$ and six axial positions with increasing distance to the bend for the tested hybrid LES/RANS turbulence models. Mesh: 2a/2e.

In Fig. 8, the performance indicators for the simulation of the SA-based and SST-based IDDES turbulence model with and without turbulent excitation at the inlet, in contrast to the SBES model, are illustrated. Compared to the former results (SA-IDDES and SST-IDDES with a steady inlet), the simulation results are enhanced regarding the L^2_{error} for all recorded planes. The turbulent excitation at the inlet leads to similar results for all hybrid models for a distance of $z > 10\,D$. This is also visible in the contour plots in Fig. 7. With unsteady turbulent inlet conditions for the IDDES models, the horseshoe shape of the profile is dissolved as with the SBES model and LDA measurement.
Regarding the performance indicator $u_{\max}$, the results are inferior to the former results with a steady inlet for a distance range till approximately $10\,D$. The swirling intensity is underestimated close to the bend with the fluctuating inlet (see Fig. 8 (b)).
The main reason for the difference is in the changed transition from the RANS to the LES region close to the bend. To put it more precisely, the main reason is due to the smaller RANS region for the simulation with the unsteady inlet condition near the bend, compare Fig. 10. The unsteady turbulent inlet results in a notably smaller RANS region close to the bend. It can be concluded that without turbulent excitation at the inlet, the separation induced by the bend is too weak to enable realistic turbulent fluctuations and a fast transition to a turbulent regime, which should result in a LES region in the separation zone. Therefore, the hybrid IDDES models require an unsteady inlet condition for this specific geometry to show an improvement compared to pure RANS results.

5. **Summary**

In this study, the performance of several RANS and hybrid LES/RANS turbulence models with different CFD solvers has been tested in terms of their ability to reproduce the flow downstream of a 90° pipe bend. The focus has been on the temporal mean profiles downstream of the bend up to approximately 31 times the pipe's diameter D. The performance of the models has been evaluated by means of two performance indicators (L^2_{error} and maximum horizontal velocity $u_{\max}$) as well as a comparison of velocity contours at six different positions downstream of the bend. For the hybrid LES/RANS models, the evaluation is extended by the comparison of the turbulent viscosity ν_t as an indicator for the RANS

and LES region.
It has been shown that the free and open source CFD software packages OpenFOAM and RapidCFD can cope with the commercial ANSYS Fluent software. For the test case of a 90° pipe bend, they yield comparable results, using the same RANS turbulence models (SA and SST).
Whether the use of a hybrid turbulence model associated with a higher computational cost is beneficial, is dependent on the investigated distance to the bend. As the RANS simulations lack the ability to dissipate the secondary motion in the flow, the rotating Dean vortices remain stronger in the flow further downstream. Additionally, the centroid of the fluid stays outside the pipe centre, and a reshaping towards a fully developed flow profile is deferred, compared to the LDA measurements. The RANS simulations are less accurate than the tested hybrid models in reproducing the flow in a pipe downstream of a 90° bend with a distance to the bend greater than approximately 10 D.
Nevertheless, the RANS simulations show slightly better results in a distance range from 2.43 to 10.7 D. In this range, the displacement of the core flow, as well as the strength of the rotation of the Dean vortices, is captured by the RANS models in an equal or even more accurate way than by the tested hybrid LES/RANS models. The best RANS model regarding the performance indicator $u_{\max}$ is the standard k-ε model, but it underestimates the displacement of the core flow towards the outer wall, leading to a higher L^2_{error}. Additionally, it shows more inaccurate results comparing the shape of the flow profile in the axial direction z, as it overpredicts the maximal axial velocity w far downstream of the bend, leading to a steeper flow profile. In terms of the performance indicator L^2_{error}, the SA model shows the best results of the tested RANS models in the vicinity of the bend.
In a downstream interval of 10.7 to 30.82 D, the hybrid SBES model surpasses the RANS models as well as the IDDES models with a steady inlet condition. This model shows good results in terms of the L^2_{error}, as an indicator of the agreement of the velocity profiles in the streamwise direction z between the simulation and the measurement. The depletion of the bend-induced disturbances (Dean vortices and shift of fluid centroid towards the outer wall) is well captured by the SBES model.
For the hybrid IDDES models, it has been found that a turbulent transient inlet condition is required to show accurate results, comparable to the SBES model for z/D >10. In the vicinity of the bend, the IDDES models show even better results than the SBES model. The improved results are mainly due to a reduced RANS region downstream of the bend.
Moreover, it has been found that for the SBES model, a fine near-wall resolution is beneficial, whereas the overall mesh resolution has a lower influence on the model's performance in terms of the L^2_{error}. For the IDDES models, no clear tendency of the influence of the grid resolution has been found, but for the coarsest mesh resolution (mesh1a), the results are not reasonable with a steady inlet.
For almost all the tested turbulence models, both RANS and hybrid LES/RANS, the best agreement between the measurement and the simulation is at position 10.7 D downstream of the bend, evaluated in terms of the L^2_{error}.

6. **Acknowledgements**

This work was supported by the Federal Ministry for Economic Affairs and Climate Action within the project EnEff:Wärme (Grant No. 03ET1498D).

Author Contributions: Conceptualisation, A.E., A.W. and M.S.; methodology, A.E., A.W. and M.S.; software, A.E., A.W. and M.S.; validation, A.E., A.W. and M.S.; formal analysis, A.E.; investigation, A.E., A.W.and M.S.; data curation, A.E., A.W. and M.S.; writing—original draft preparation, A.E.; writing—review and editing, A.E., A.W., M.S., T.E. and K.O.; visualisation, A.E.; supervision, T.E.; funding acquisition, T.E. . All authors have read and agreed to the published version of the manuscript.

Appendix A. Additional Results

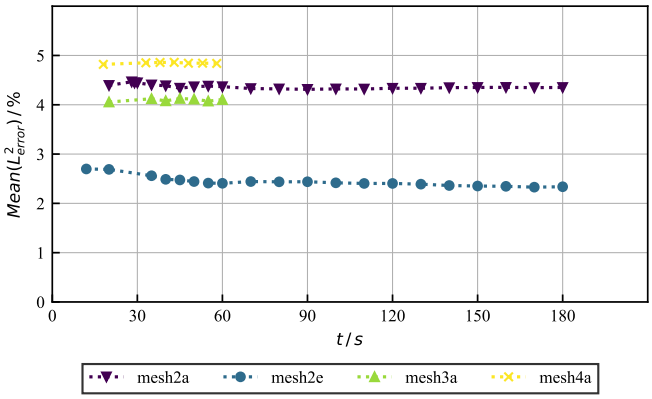

Figure 11. Mean L^2_{error} over averaging time t. Turbulence model: SA-IDDES. Solver: RCFD.

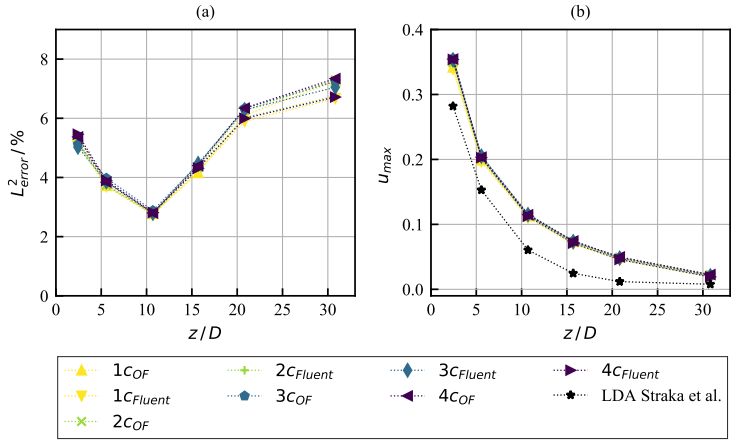

Figure 12. Comparison of different mesh resolutions according to Tab. 2. Turbulence model: SST (a) L^2_{error} and (b) maximum horizontal velocity $u_{\max}$ over the normalised distance downstream of the bend z/D. For better visualisation, the values evaluated at the marked positions are connected by lines. LDA measurements by Straka et al. [30].

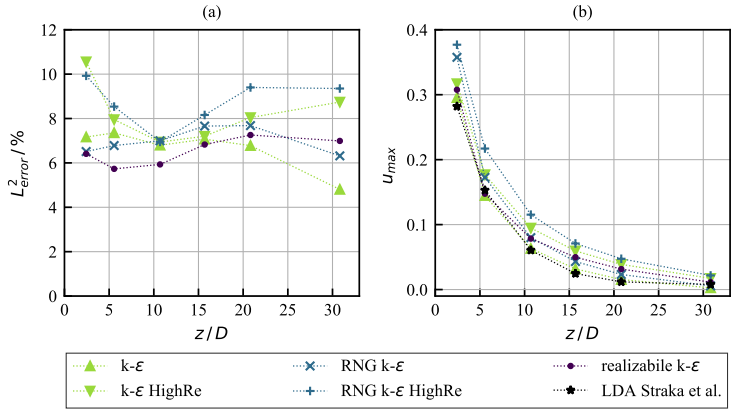

Figure 13. Comparison of different ε-based RANS turbulence model. (a) L^2_{error} and (b) maximum horizontal velocity $u_{\max}$ over the normalised distance downstream of the bend z/D. For better visualisation, the values evaluated at the marked positions are connected by lines. LDA measurements by Straka et al. [30].

References

[1] P. Welahettige and K. Vaagsaether, "Comparison of OpenFOAM and ANSYS Fluent," in *Proceedings of the 9th EUROSIM 2016 & the 57th SIMS 2016*, 2016, http://dx.doi.org/10.3384/ecp171421005.

[2] M. Balogh, A. Perenty, and C. Benocci, "RANS simulation of ABL flow over complex terrains applying an Enhanced k-ε model and wall function formulation: Implementation and comparison for fluent and OpenFOAM," *Journal of Wind Engineering and Industrial Aerodynamics*, vol. 104-106, pp. 360–368, 2012, https://doi.org/10.1016/j.jweia.2012.02.023.

[3] D. A. Lysenko, I. S. Ertesvg, and K. E. Rian, "Modeling of turbulent separated flows using OpenFOAM," *Computers & Fluids*, vol. 80, pp. 408–422, 2013, https://doi.org/10.1016/j.compfluid.2012.01.015.

[4] simFlow, RapidCFD, https://sim-flow.com/rapid-cfd-gpu/.

[5] D. Jasiński, "Adapting OpenFOAM for massively parallel GPU architecture," *The 3rd OpenFOAM User Conference 2015, Stuttgart - Germany*, 2015.

[6] OpenFOAM 2.3.1, https://openfoam.org/release/2-3-1/.

[7] A. Nocente, T. Arslan, D. Jasinski, and T. K. Nielsen, "A Study of Flow inside a Centrifugal Pump: High Performance Numerical Simulations Using GPU cards," in *16th International Symposium on Transport Phenomena and Dynamics of Rotating Machinery*, 2016.

[8] D. Molinero, S. Galván, J. Pacheco, and N. Herrera, "Multi GPU Implementation to Accelerate the CFD Simulation of a 3D Turbo-Machinery Benchmark Using the RapidCFD Library," *Torres M., Klapp J. (eds) Supercomputing. ISUM 2019. Communications in Computer and Information Science*, vol. 1151, pp. 173–187, 2019, https://doi.org/10.1007/978-3-030-38043-4_15.

[9] V. Kurashov, "Modification of RhoCentralFoam Solvers Based on OpenFOAM and RapidCFD to Calculate High-Speed Flows. Speed Comparison of GPU and CPU Solvers," *Physical-Chemical Kinetics in Gas Dynamics*, vol. 17, no. 4, pp. 1–11, 2016, http://chemphys.edu.ru/issues/2016-17-4/articles/662/.

[10] W. R. Dean, "XVI. Note on the motion of fluid in a curved pipe," *The London, Edinburgh, and Dublin Philosophical Magazine and Journal of Science, 4:20*, pp. 208–223, 1927, https://doi.org/10.1080/14786440708564324.

[11] C. Carlander and J. Delsing, "Installation effects on an ultrasonic flow meter," in *FLOMEKO*, 1998, pp. 149–154.

[12] A. Hilgenstock and R. Ernst, "Analysis of installation effects by means of computational fluid dynamics," *Flow Measurement and Instrumentation*, vol. 7, pp. 161–171, 1996.

[13] E. Kelner, "Flow Meter Installation Effects," in *American School of Gas Measurement Technology*, 2007, http://asgmt.com/wp-content/uploads/pdf-docs/2007/1/033.pdf.

[14] G. E. Mattingly and T. T. Yeh, "Flowmeter installation effects due to several elbow configurations," in *North American Fluid Flow Measurement Conference (NAFFMC)*, 1990.

[15] A. Weissenbrunner, A. Fiebach, S. Schmelter, M. Bär, P. Thamsen, and T. Lederer, "Simulation-based determination of systematic errors of flow meters due to uncertain inflow conditions," *Flow Measurement and Instrumentation*, vol. 52, pp. 25–39, 2016, http://dx.doi.org/10.1016/j.flowmeasinst.2016.07.011.

[16] G. Wendt, B. Mickan, R. Kramer, and D. Dopheide, "Systematic investigation of pipe flows and installation effects using laser Doppler anemometry - Part I. Profile measurements downstream of several pipe configurations and flow conditioners," *Flow Meas. Instrum.*, vol. 7, pp. 141–149, 1996.

[17] J. Frhlich and D. von Terzi, "Hybrid LES/RANS methods for the simulation of turbulent flows," *Progress in Aerospace Sciences*, vol. 44, pp. 349–377, 2008, https://doi.org/10.1016/j.paerosci.2008.05.001.

[18] J. Kim, M. Yadav, and S. Kim, "Characteristics of Secondary Flow Induced by 90-Degree Elbow in Turbulent Pipe Flow," *Engineering Applications of Computational Fluid Mechanics*, vol. 8, no. 2, pp. 229–239, 2014, https://doi.org/10.1080/19942060.2014.11015509.

[19] P. Dutta and N. Nandi, "Effect of Reynolds Number and Curvature Ratio on Single Phase Turbulent Flow in Pipe Bends," *Mechanics and Mechanical Engineering*, vol. 19, no. 1, pp. 5–16, 2015.

[20] P. Dutta, S. K. Saha, N. Nandi, and N. Pal, "Numerical study on flow separation in 90° pipe bend under high Reynolds number by k-ε modelling," *Engineering Science and Technology, an International Journal*, vol. 19, no. 2, pp. 904–910, 2016, https://doi.org/10.1016/j.jestch.2015.12.005.

[21] R. Rhring, S. Jakirli, and C. Tropea, "Comparative computational study of turbulent flow in a 90° pipe elbow," *International Journal of Heat and Fluid Flow*, vol. 55, pp. 120–131, 2015, https://doi.org/10.1016/j.ijheatfluidflow.2015.07.011.

[22] C. Carlsson, E. Alenius, and L. Fuchs, "Swirl switching in turbulent flow through 90° pipe bends," *Physics of Fluids*, vol. 27, no. 8, pp. 085 112–1–085 112–17, 2015, https://doi.org/10.1063/1.4928971.

[23] F. Rtten, W. Schrder, and M. Meinke, "Large-eddy simulation of low frequency oscillations of the Dean vortices in turbulent pipe bend flows," *Physics of Fluids*, vol. 17, no. 3, pp. 035 107–1–035 107–11, 2005, https://doi.org/10.1063/1.1852573.

[24] R. Tunstall, D. Laurence, R. Prosser, and A. Skillen, "Benchmarking LES with wall-functions and RANS for fatigue problems in thermalhydraulics systems," *Nuclear Engineering and Design*, vol. 308, pp. 170–181, 2016, https://doi.org/10.1016/j.nucengdes.2016.08.022.

[25] Z. Wang, R. rl, P. Schlatter, and Y. M. Chung, "Direct numerical simulation of a turbulent 90° bend pipe flow," *International Journal of Heat and Fluid Flow*, vol. 73, pp. 199–208, 2018, https://doi.org/10.1016/j.ijheatfluidflow.2018.08.003.

[26] L. H. O. Hellstrm, A. Sinha, and A. J. Smits, "Visualizing the very-large-scale motions in turbulent pipe flow," *Physics of Fluids*, vol. 23, pp. 011 703–1–011 703–4, 2011, https://doi.org/10.1063/1.3533016.

[27] C. Brcker, "A time-recording DPIV-study of the swirl switching effect on a 90° bend flow," *Proc. 8th International Symposium on Flow Visualization, Sorrento (NA), Italy*, pp. 171.1–171.6, 1998.

[28] Y. Iwamoto, M. Kondo, H. Minamiura, M. Tanaka, and H. Yamano, "Unsteady Flow Characteristics in a 90 Degree Elbow Affected by Developed, Undeveloped and Swirling Inflow Conditions," *Journal of Fluid Science and Technology*, vol. 7, no. 3, pp. 315–328, 2012, https://doi.org/10.1299/jfst.7.315.

[29] Y. Iwamoto and H. Yamano, "Unsteady wall pressure characteristics of a 90 degree elbow in high Reynolds number," *Journal of Fluid Science and Technology*, vol. 9, no. 3, p. JFST0055, 2014, https://doi.org/10.1299/jfst.2014jfst0055.
[30] M. Straka, C. Koglin, and T. Eichler, "Segmental orifice plates and the emulation of the 90°-bend," *tm - Technisches Messen*, vol. 87, no. 1, pp. 18–31, 2020, https://doi.org/10.1515/teme-2019-0120.
[31] D. C. Wilcox, *Turbulence Modeling for CFD*. DCW Industries, Inc., 2006.
[32] F. R. Menter, "Two-Equation Eddy-Viscosity Turbulence Models for Engineering Applications," *AIAA Journal*, vol. 32, no. 8, pp. 1598–1605, 1994, https://doi.org/10.2514/3.12149.
[33] P. R. Spalart and S. R. Allmaras, "A One-Equation Turbulence Model for Aerodynamic Flows," in *30th Aerospace Sciences Meeting and Exhibit*. AIAA 1992-439, 1994, https://doi.org/10.2514/6.1992-439.
[34] J. Smagorinsky, "General circulation experiments with the primitive equations," *Monthly Weather Review*, vol. 91, pp. 99–164, 1963.
[35] F. R. Menter, "Best Practice: Scale-Resolving Simulations in ANSYS CFD," 2012.
[36] M. Straka, A. Fiebach, C. Koglin, and T. Eichler, "Hybrid simulation of a segmental orifice plate," *Flow Measurement and Instrumentation*, vol. 60, pp. 124–133, 2018, https://doi.org/10.1016/j.flowmeasinst.2018.02.006.
[37] M. L. Shur, P. R. Spalart, M. K. Strelets, and A. K. Travin, "A hybrid RANS-LES approach with delayed-DES and wall-modelled LES capabilities," *International Journal of Heat and Fluid Flow*, vol. 29, no. 6, pp. 1638–1649, 2008, https://doi.org/10.1016/j.ijheatfluidflow.2008.07.001.
[38] M. S. Gritskevich, A. V. Garbaruk, J. Schtze, and F. R. Menter, "Development of DDES and IDDES Formulations for the k-ω Shear Stress Transport Model," *Flow Turbulence Combust*, vol. 88, pp. 431–449, 2012, https://doi.org/10.1007/s10494-011-9378-4.
[39] T. Eichler, "Messunsicherheit eines LDV-Systems. Qualitätsmanagement-Arbeitsanweisung 7.6-AA-2.1. Physikalisch-Technische Bundesanstalt," 2009.
[40] ANSYS ICEM CFD 19.3, "Help Manual."
[41] M. Straka, "Vergleich realer und synthetisch generierter Strmungszustnde in Rohrleitungen mittels numerischer und laseroptischer Verfahren," Ph.D. dissertation, Technische Universitt Berlin, 2021, https://depositonce.tu-berlin.de/handle/11303/13786.
[42] ANSYS Fluent Release 19.3, https://www.ansys.com/products/fluids/ansys-fluent.
[43] OpenFOAM®v1812, https://www.openfoam.com/releases/openfoam-v1812/.
[44] F. Mathey, D. Cokljat, J. P. Bertoglio, and E. Sergent, "Specifications of LES inlet boundary condition using vortex method," in *4th International Symposium on Turbulence, Heat and Mass Transfer*, 2003.
[45] F. Menter and T. Esch, "Elements of Industrial Heat Transfer Predictions," *16th Brazilian Congress of Mechanical Engineering (COBEM)*, 2001.
[46] D. B. Spalding, "A single formula for the law of the wall," *Transactions of the ASME, Series E: Journal of Applied Mechanics*, vol. 28, pp. 455–458, 1961.
[47] K. Sudo, M. Sumida, and H. Hibara, "Experimental investigation on turbulent flow in a circular-sectioned 90-degree bend," *Experiments in Fluids*, vol. 25, pp. 42–49, 1998, https://doi.org/10.1007/s003480050206.